In vivo Characterization and Numerical Simulation of Prostate Properties for Non-Thermal Irreversible Electroporation Ablation

Robert E Neal II,[1]* Jeremy L Millar,[2] Helen Kavnoudias,[1] Peter Royce,[3] Franklin Rosenfeldt,[4] Alan Pham,[5] Ryan Smith,[2] Rafael V Davalos,[6] and Kenneth R Thomson[1]

[1]*Department of Radiology, The Alfred Hospital, Melbourne, VIC, Australia*
[2]*William Buckland Radiotherapy Centre, The Alfred Hospital, Melbourne, VIC, Australia*
[3]*Department of Urology, The Alfred Hospital, Monash University, Melbourne, VIC, Australia*
[4]*Department of Surgery, The Alfred Hospital, Melbourne, VIC, Australia*
[5]*Department of Anatomical Pathology, The Alfred Hospital, Melbourne, VIC, Australia*
[6]*School of Biomedical Engineering and Sciences, Virginia Tech, Blacksburg, VA*

BACKGROUND. Irreversible electroporation (IRE) delivers brief electric pulses to attain non-thermal focal ablation that spares vasculature and other sensitive systems. It is a promising prostate cancer treatment due to sparing of the tissues associated with morbidity risk from conventional therapies. IRE effects depend on electric field strength and tissue properties. These characteristics are organ-dependent, affecting IRE treatment outcomes. This study characterizes the relevant properties to improve treatment planning and outcome predictions for IRE prostate cancer treatment.

METHODS. Clinically relevant IRE pulse protocols were delivered to a healthy canine and two human cancerous prostates while measuring electrical parameters to determine tissue characteristics for predictive treatment simulations. Prostates were resected 5 hr, 3 weeks, and 4 weeks post-IRE. Lesions were correlated with numerical simulations to determine an effective prostate lethal IRE electric field threshold.

RESULTS. Lesions were produced in all subjects. Tissue electrical conductivity increased from 0.284 to 0.927 S/m due to IRE pulses. Numerical simulations show an average effective prostate electric field threshold of 1072 ± 119 V/cm, significantly higher than previously characterized tissues. Histological findings in the human cases show instances of complete tissue necrosis centrally with variable tissue effects beyond the margin.

CONCLUSIONS. Preliminary experimental IRE trials safely ablated healthy canine and cancerous human prostates, as examined in the short- and medium-term. IRE-relevant prostate properties are now experimentally and numerically defined. Importantly, the electric field required to kill healthy prostate tissue is substantially higher than previously characterized tissues. These findings can be applied to optimize IRE prostate cancer treatment protocols. *Prostate* © 2014 Wiley Periodicals, Inc.

KEY WORDS: **prostate cancer; preclinical trials; targeted therapy; translational research; IRE; finite element modeling**

INTRODUCTION

Prostate cancer is the most common internal cancer in men [1]. Improved surveillance, including prostate-specific antigen (PSA) monitoring, has generated a surge of new diagnoses [2], with a majority as organ-confined disease [3,4]. A diverse range of treatment options include systemic hormone therapy, chemotherapy, and

Grant sponsor: Flack Trustees; Grant sponsor: The Coulter Foundation; Grant sponsor: Whitaker International Program.

*Correspondence to: Robert E. Neal II, PhD, Radiology Research Unit, Department of Radiology, 1st Floor Philip Block, The Alfred Hospital, 55 Commercial Road, Melbourne, VIC 3004, Australia.
E-mail: robert.neal@alfred.org.au
Received 20 August 2013; Accepted 8 November 2013
DOI 10.1002/pros.22760
Published online in Wiley Online Library (wileyonlinelibrary.com).

immunotherapy; as well as localized interventions such as external beam and internal source radiation, surgical excision, or thermal ablation [2,5,6]. Unfortunately, current prostate cancer treatments carry significant complication risk and substantial morbidity including urinary incontinence, rectal injury, and erectile dysfunction [2,5].

The majority of men diagnosed with prostate cancer will not die from their disease [7], leading some to suggest active surveillance for low-risk prostate cancer patients. The large number of locally confined, low-risk prostate cancer diagnoses has also driven efforts to reduce treatment invasiveness, such as robot-assisted prostatectomies, and targeted techniques such as cryoablation and high-intensity focused ultrasound [5,8]. Although evidence suggests some of these techniques can reduce morbidity relative to open radical prostatectomies and radiation [5,8], focal therapies still carry significant risks due the close proximity of prostate tumors to sensitive structures including the urethra, bowel, and neurovascular bundles [5]. Mitigating such risks can reduce therapeutic efficacy for neoplastic cells in the most sensitive regions. Therefore, continuing research aims to refine these techniques and develop novel approaches for the large number of low-risk, locally confined prostate cancers. Such a technique should attain complete tumor control without damaging important structures, thus reducing treatment-associated morbidity.

Irreversible electroporation (IRE) is an emerging non-thermal focal ablation technique. It uses needle electrodes ($\sim$1 mm diameter) placed into or around a targeted volume of tissue to deliver a series of brief ($\sim$100 μsec) but intense (1–3 kV) electric pulses. These pulses alter cellular transmembrane potentials within the affected volume, leading to membrane destabilization and nanoscale defects [9]. When the collective energy from pulse series is sufficient (intensity, pulse length, number of pulses, repetition rate) the cell cannot recover from these defects and dies in a non-thermal manner [10].

IRE non-thermal tissue ablation exhibits multiple benefits as a minimally invasive approach for tumor treatment [11]. There is a sub-millimeter demarcation between destroyed and unaffected cells that is controllable based on electrode arrangements and pulse parameters, with a treatment volume that exhibits rapid lesion creation and resolution [12,13]. Destroyed volume correlates with the electric field distribution [14], enabling treatment planning; while changes to tissue properties enable treatment monitoring in real-time [15,16]. Treatments are unaffected by heat-sink blood perfusion, and emerging evidence suggests electroporated tissue may invoke a complementary immune response [17–19]. Importantly, the pulses do not affect the extracellular matrix; sparing sensitive structures including the major vasculature, neurovascular bundles, and ductal systems [13,20,21]. This enables IRE to be used with low morbidity risk in regions too dangerous for resection or other focal techniques.

IRE has achieved promising tumor treatment results in small animals [22,23]. Veterinary case studies demonstrate its utility to treat complex tumors in sensitive regions; including a large sarcoma encompassing the sciatic nerve and major blood vessels [24], and a brain tumor [25]. A phase I human safety study on tumors that failed or were ineligible for other therapies achieved complete ablation in 49 of 69 tumors in the liver, kidney, and lung [26]. New evidence suggests IREs potential as a complementary approach in pancreas cancer treatments [27,28].

IRE is a promising treatment for organ-confined prostate cancer. IREs non-thermal cell death mechanism should enable complete destruction of the targeted tissues without damaging the vital adjacent structures. Currently, literature regarding IRE prostate applications remains limited. The effects of varying pulse parameters were examined using in vitro prostate cancer cells pulsed in suspension [29]. An in vivo study examined canine prostate response up to 14 days post-IRE, which showed the ability to ablate volumes of healthy prostate without damaging the neurovascular bundles or urethra [13], both of which are critical for patient quality of life following prostate cancer treatment [30].

Although IRE has great potential in the treatment of numerous focal diseases, its effects remain poorly characterized for many tissues. IRE effects relate to electric field distribution, which is dependent on the conductivity distribution in the targeted region [31]. Furthermore, these properties are dynamic and will change in response to the pulsed electric fields [32]. Finally, tissue microenvironment and cellular variability will affect lethal electric field thresholds, and therefore ablation volumes for a given pulse protocol. For example, a tumor was ablated while the immediately adjacent muscle cells recovered viability [24]. While clinical utilization of IRE remains in its infancy, it is important to understand how the electrophysical and biological characteristics of tissue response will change in different applications.

In this study, we build on [33] to characterize the relevant prostate tissue electrical properties and response to IRE pulsed electric fields from in vivo healthy canine prostate and human prostate cancer. Numerical simulations are also used to calibrate an effective lethal electric field threshold to determine the susceptibility of healthy prostate tissue to IRE. These parameters are vital in developing accurate numerical

simulations to optimize treatment protocols that ensure complete destruction of the targeted zone while preserving as much healthy tissue as possible, which is critical for achieving ideal patient outcomes.

MATERIALS AND METHODS

Canine Experiment

This study was approved by the institutional animal ethics committee. A male canine weighing approximately 30 kg was premedicated with acetylpromazine (0.1 mg/kg), atropine (0.05 mg/kg), and morphine (0.2 mg/kg) prior to general anesthesia induced with propofol (6 mg/kg, then 0.5 mg/kg/min) and maintained with inhaled isofluorane (1–2%). Anesthetic depth was monitored using a bispectral index monitor (Covidien, Dublin, Ireland) to measure extent of EEG brain activity. Pancuronium bromide (0.1–0.3 mg/kg) was administered to reduce electric pulse induced muscular contraction.

Under anesthesia, a midline incision was made inferiorly and the prostate was accessed. Two modified single-polarity NanoKnife (Angiodynamics, Queensbury, NY) 18 gauge needle electrodes (1 cm separation and 0.5 cm exposed length) were inserted into the prostate on opposing sides of the urethra (Fig. 1A). An ECM830 generator (Harvard Apparatus, Cambridge, MA) delivered an initial 100 μsec pre-pulse of 50 V between the electrodes (50 V/cm voltage-to-distance ratio) to determine a baseline tissue conductivity, which is below the threshold for electroporation-induced conductivity changes. Electrical current was measured with a Tektronix TCP305 electromagnetic induction current probe connected to a TCPA300 amplifier (both Tektronix, Beaverton, OR). A Protek DS0-2090 USB computer-interface oscilloscope provided current measurements on a laptop using the included DSO-2090 software (both GS Instruments, Incheon, Korea) (Fig. 1B). The 50 V between the 1 cm separated electrodes exposes the bulk tissue to electric fields below the electroporation threshold. This enables determination of a baseline tissue conductivity, where the intact cellular membranes behave as dielectrics, constraining current flow through the interstitial fluid [9].

Following the pre-pulse, a clinical IRE-relevant ablation pulse sequence was performed between the two electrodes using a series of 100 pulses, each

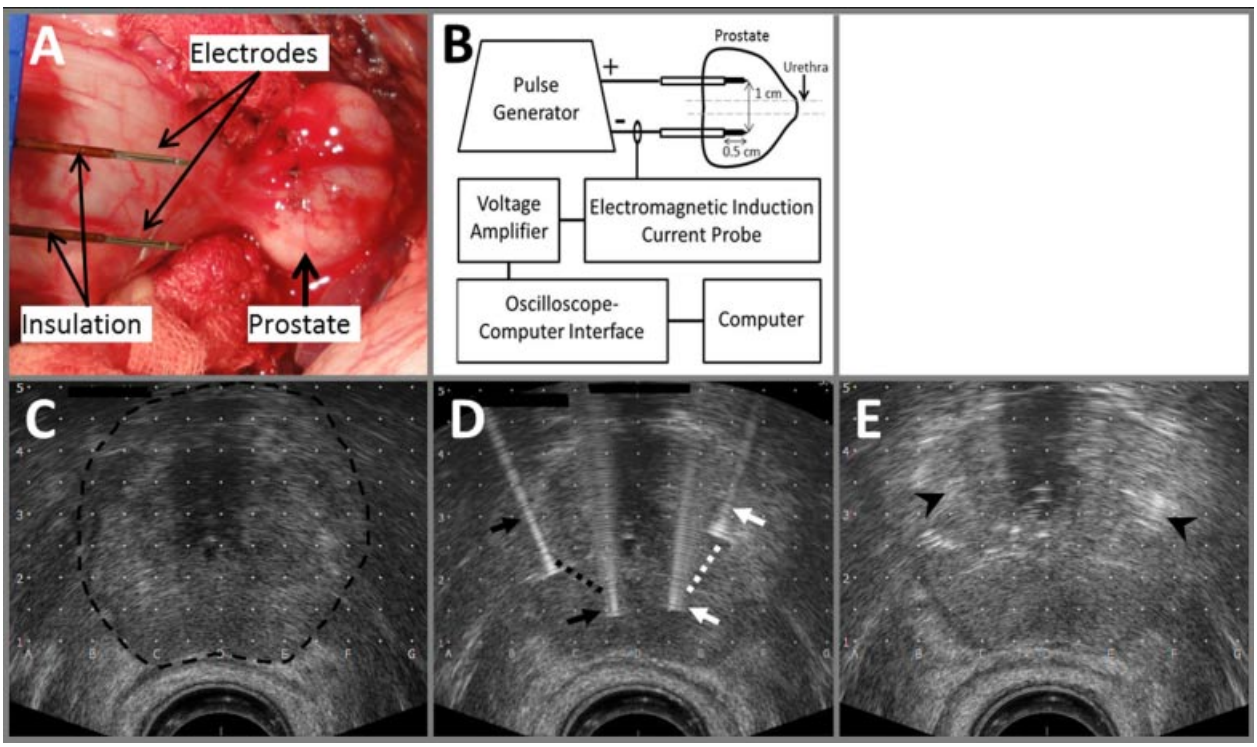

Fig. 1. Canine experiment setup and human trial ultrasound volume studies. **A**: Electrodes immediately prior to prostate insertion (note, pictured with 1 cm exposure length). **B**: Schematic of experimental equipment setup. **C**–**E**: Transverse ultrasound images of prostate (dark region, dashed outline) from human trial (C) prior to electrode insertion, (D) immediately following electrode insertion, showing the four electrodes inserted as two pairs (white and black arrow pairs) with pulses delivered between dashed lines for two ablations, and (E) 35 min following IRE electric pulses, showing gas formation (arrowheads).

100 μsec long, delivered at a rate of 1 pulse per second with a strength of 1,250 V (1,250 V/cm voltage-to-distance ratio). The pulse parameters were selected for their relevance to clinical utilization and significant prior experimental characterizations. The 1 cm separation electrodes delivering an applied voltage of 1250 V was selected to create a contiguous ablation that remained confined within the prostate boundaries. It was determined based on predictions using tissue properties for previously characterized tissues with lethal electric field thresholds of 500–650 V/cm [14,34].

Secondary pulse parameters (total pulses, pulse length, and pulse repetition rate) were selected within ranges commonly employed in prior IRE literature, and were designed to attain reliable ablations while remaining below thresholds that may induce significant thermal damage [22,35,36]. The use of 100 total pulses was selected because the maximum pulse number protocol examined in Ref. [22], 80 pulses, achieved the greatest complete ablation rate in cutaneous murine tumors, while [29] suggests a reduction in required electric field for greater pulse numbers in vitro.

Following pulse delivery, the electrodes were removed and the animal was maintained on anesthesia for an additional 4 hr to allow adequate lesion development prior to humane euthanasia [37] via pentobarbital overdose. The prostate was harvested and preserved in buffered formalin before sectioning into 2 mm slices for measuring lesion dimensions.

Human Safety Trials

Two human prostate ablation case trials were performed under approval from the Institutional Review Board as part of trial ACTRN12612000523808. In these cases, two patients underwent IRE procedures either 3 or 4 weeks prior to their prescribed prostatectomy for carcinoma. Eligibility criterion for the study required that the patients had disease confined to the prostate (clinical stage T1c and T2a), an Anesthesia Surgical Assignment category IV or greater, had no prostate calcification >5 mm, and no history of bladder neck contracture, inflammatory bowel disease, bleeding disorder, or other concurrent debilitating disease. Patients were fully informed about the research nature of the IRE study and understood that the IRE procedure was not designed to have any beneficial clinical effect.

For the procedure, patients received general anesthetic and muscular blockade as described in Ref. [38]. Patients were placed in the lithotomy position as used for prostate brachytherapy. Transrectal ultrasound (US) determined prostate location relative to the needle guidance system (Fig. 1C) before inserting a total of four, 18 G single-polarity NanoKnife (Angiodynamics) needle electrodes into each prostate, two per lobe (Fig. 1D). Separations for each intralobe electrode pair were measured on US, and electric pulse strength was set for the desired voltage-to-distance ratio.

The NanoKnife generator system (Angiodynamics) delivered a series of electric pulses at a cardiac autosynchronous rate using the Accusync ECG trigger (Accusync, Milford, CT) to reduce the risk of pulse-induced cardiac arrhythmia. Pulses were delivered only between electrodes within the same lobe, producing two ablations per human subject, with the protocol for each ablation shown in Table I. The secondary pulse parameters of 90 total pulses, each 70 μsec long for the human trials were based on previous clinical reports in other tissues [26,27,39], the NanoKnife generator manufacturer's recommendations, and ethics approval criterion. This study was designed to confirm the safety of IRE in the prostate and to characterize the unique prostate ablation susceptibility. Therefore, the electrode exposure lengths, separation distances, and placements were intentionally selected to produce ablation margins contained completely within the bulk healthy prostate tissue. The applied voltages were also targeted at this objective, and were selected to produce contiguous ablations within the objective region of tissue based on predictions from previously characterized tissues, and to ensure electri-

TABLE I. Experimental Electric Pulse Parameters for Canine and Human Trials

Trial	Subject	Lesion	Exposure length (cm)	Separation distance (cm)	Applied voltage (V)	Voltage–distance ratio (V/cm)	Pulse length (μsec)	Pulse number	Median current (A)	Post-IRE tissue removal
1	Canine	—	0.5	1	1,250	1,250	100	100	5	4 hours
2	Human	1	1	1.2	1,800	1,500	70	90	12	3 weeks
3	Human	2	1	1.4	2,100	1,500	70	90	19	3 weeks
4	Human	1	1.5	1.5	2,625	1,750	70	90	32	4 weeks
5	Human	2	1.5	1.5	2,625	1,750	70	90	34	4 weeks

cal currents within the upper limits of the generator's capacity (50 A).

Post-IRE US detected immediate changes including substantial gas formation near electrode insertions (Fig. 1E), after which the patients recovered from anesthesia uneventfully. Patients then underwent their regularly scheduled prostatectomies. Prostates were preserved in 10% neutral buffered formalin and sectioned into 4 mm thick slices for attaining pathology sections stained with Hematoxylin and Eosin for histological determination of lesion dimensions and IRE effects.

Numerical Modeling

Treatment effects can be correlated with the electric field distribution, which can be predicted with numerical solutions using finite element modeling [14]. This was employed with the canine and human experimental data to calibrate the electrical properties of prostate tissue and its response to the IRE. A three-dimensional finite element model was created using Comsol Multiphysics 3.5a (Comsol, Stockholm, Sweden) to simulate the experimental protocols. The canine prostate was simulated as a 2.3 cm × 2.1 cm × 1.8 cm ellipsoid. Two electrodes, each 1 mm in diameter and 0.5 cm long, were placed within opposite sides of the domain. The urethra was represented as a 0.5 cm diameter cylinder running parallel to the electrodes at a position approximated from the sectioned prostate image. Human prostates were both represented as 4.8 cm × 4.2 cm × 3.4 cm ellipsoids, based on the resected prostate dimensions. Electrodes were placed at positions approximated from the US images, with separations matching those used when setting pulse parameters. The urethra was not included in human simulations due to the determination that urethra presence did not significantly affect canine simulations (not shown).

Tissue Electrical Properties

The electric field is solved from the governing equation:

$$\nabla (\sigma \nabla \phi) = 0 \tag{1}$$

where σ is the electrical conductivity of the tissue and ϕ is the electric potential. Models were solved considering dynamic tissue electrical conductivity, which accounts for electroporation-induced conductivity increases due to improved electrolyte mobility, and has been shown to more accurately predict tissue behavior when determining ablation shapes and volumes [40,41]. This dynamic conductivity, $\sigma(E)$, as a function of electric field, E, was solved based on the results of [42] from ex vivo porcine renal tissue experiments, using the asymmetrical sigmoid Gompertz curve function

$$\sigma(E) = \sigma_0 + (\sigma_{max} - \sigma_0) \cdot \exp[-A \cdot \exp(-B \cdot E)] \tag{2}$$

where σ_0 and σ_{max} are the minimum (no electroporation) and plateau (fully saturated) electrical conductivities within a single pulse. A and B are unitless coefficients that vary with pulse length, t. All models assumed a 100 μsec long pulse, where $A = 3.212$ and $B = 0.002543$.

To determine σ_0 and σ_{max} for each trial, a constant conductivity was first adjusted until the simulated electrical current density over the electrode boundaries matched pre-pulse experimental current, which was below the threshold for any significant baseline tissue conductivity effects due to electroporation. Following this, the dynamic conductivity function (2) was solved while adjusting σ_{max} until the modeled and experimental current matched. Urethra properties were set to $\sigma_0 = 0.203$ and $\sigma_{max} = 0.337$ S/m, based on the *β-dispersion* hypothesis [42] and properties of bladder at 10 Hz (σ_0) and 500 MHz (σ_{max}) [43].

Ablations Lesions Used to Calibrate Lethal Electric Field Threshold

The harvested prostates were sectioned in order to determine the size of the IRE ablation lesions. In the canine case, gross pathology was used to determine the maximum width and height of each separate lesion found at the electrode insertion location, and total ablation volume was calculated by integrating lesion area dimensions over all section slices. The human prostates were examined for total affected volumes based on histological integration of prostate sections. The electric field distributions from the individually modeled IRE trials were correlated with these measured lesion dimensions to calibrate which electric field strength was sufficient to kill the prostate tissue in each case. By determining the strength of electric field required for ablation, treatment planning models that simulate electric field distributions may be used to predict ablation lesion dimensions for IRE protocols with different electrode configurations and applied voltages, thus enabling accurate protocol optimization.

RESULTS

Canine Experiment

The canine prostate ablation was performed without incident. The 50 V pre-pulse between the electrodes generated a 0.0975 A electrical current, constant

throughout the pulse duration, suggesting no significant electroporation or thermal change to tissue properties. Electrical current from the final 80–100 μsec of electrical pulse length was averaged over pulses 1–10, 40–50, and 90–100 for the 100 pulse 1250 V trial, giving a current of 4.81 ± 0.421 A (mean ± SD). Macroscopic pathology showed that the pulse parameters for the single ablation procedure produced two distinct ablation zones at the locations of electrode insertion rather than a contiguous lesion. Dimensions of the two zones are reported in Ref. [30], showing average lesions widths and heights of 0.64 and 0.63 cm, respectively, based on hemorrhagic regions shown from histology to correlate with the regions of cellular necrosis.

HumanTrials

Two patients underwent the preliminary IRE procedure used in this study. The patients were aged 64 and 57, had Gleason scores of 7 (3 + 4) and 6 (3 + 3) and PSA levels of 5.4 and 4.3 ng/ml, respectively, and met the additional eligibility requirements outlined in the Methods section. Both patients received IRE electric pulse delivery and were discharged with an intraurethral catheteter that remained in situ for up to 10 days. Both patients experienced mild hematuria after the procedure and cytoscope, and recovered in the post-IRE period without any other serious adverse event. Their prostatectomies were performed at 3 or 4 weeks post-IRE without complication. The NanoKnife generator does not report pre-pulse electrical currents. Median full-strength pulse currents are reported in Table I.

Histology showed regions of tissue necrosis surrounding the electrodes, all of which were contained within the healthy prostatic parenchyma. A variable extent of reactive stromal fibrosis and regenerative change in epithelial lining of prostatic ducts were observed surrounding the necrotic focus (Fig. 2A). Inflammatory infiltrate was present (Fig. 2B), while squamous metaplasia and hemosiderin deposition was noted near the hemorrhagic margins (Fig. 2D and E). Reconstructing histologically determined IRE-altered prostate regions resulted in total volumes of 1.14 and 2.46 cm^3 for patient trials one and two, respectively.

Numerical Simulations

A representative three dimensional finite element volumetric mesh for the model setup can be seen in Figure 3A, which represented the canine prostate. The 50 V prepulse static conductivity model used to simu-

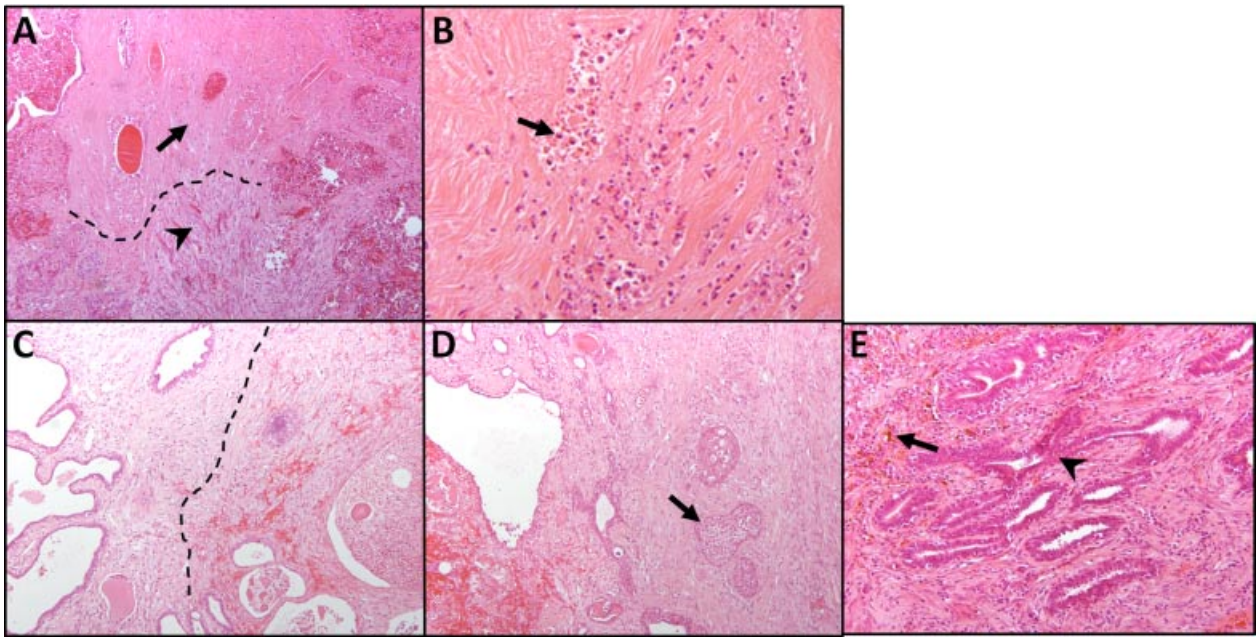

Fig. 2. Human prostate IRE histology, hemotoxylin and eosin. **A**: Delineation (dashed line) between completely necrotic upper region (arrow) and parenchyma undergoing reactive fibrosis with a proliferation of spindled fibroblasts (arrowhead), 100×. **B**: Completely necrotic region with neutrophilic inflammatory infiltrate (arrow), 200×. **C**: Delineation (dashed line) between viable tissue (left) and reactive fibrosis and hemorrhage (right), 100×. **D**: Boundary with hemorrhagic region, with viable tissue (right) showing prostatic duct squamous metaplasia (arrow), 100×. **E**: Hemosiderin deposition within surrounding stroma (arrow) beyond visible lesion margins with regenerative prostatic duct changes noted (arrowhead), 100×.

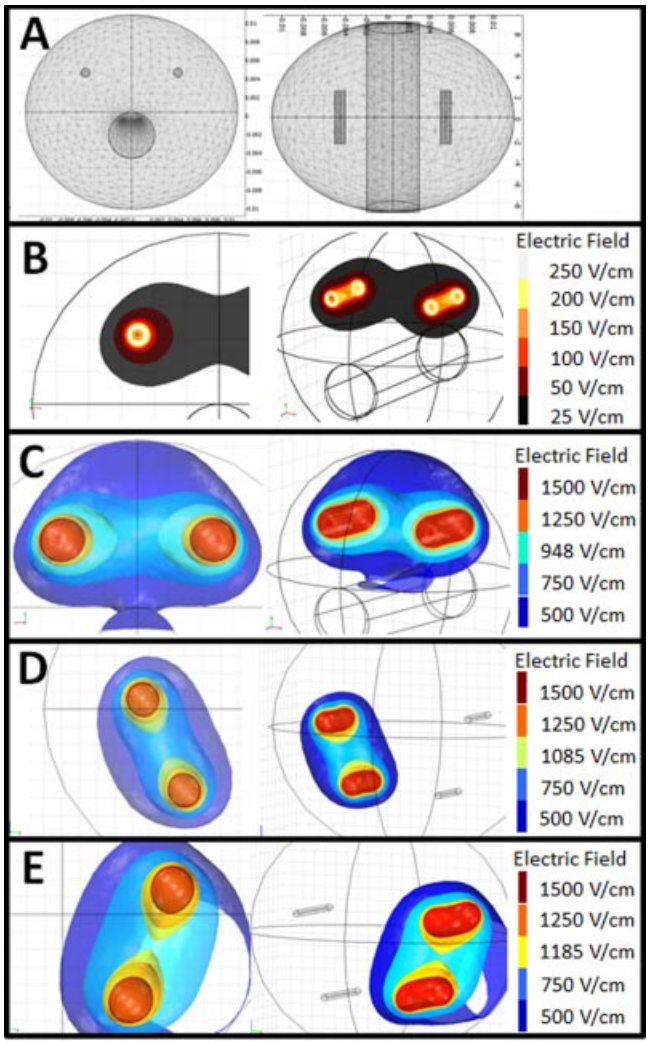

Fig. 3. IRE pulse numerical model geometries and simulation results. **A**: Representative Comsol domain, showing three dimensional finite element model volume to represent prostate, urethra, and electrode locations for the canine trial. **B**–**E**: (**Left**) Perpendicular and (**Right**) isometric views of electric field distribution (V/cm) for IRE pulses in (B and C) experimental canine subject and (D and E) human patients. B: Canine 50 V pre-pulse with static conductivity to determine σ_0. C: Canine simulation at experimental voltage. D–E: Human patient simulation results for ablations (D) one in the first patient and (E) both ablations in the second patient (due to having identical experimental parameters). Note the middle electric field outlined in each is based on matching the average lesion diameters for the canine trial (943 V/cm) as well as pathologically measured total lesion volumes for both human trials (1,085 and 1,185 V/cm).

late the canine prepulse (Fig. 3B) determined a baseline electrical conductivity of $\sigma_0 = 0.284$ S/m. This baseline conductivity was used for all models in the $\sigma(E)$ function because prepulse data were not collected from the human trials using the Nanoknife, making the canine trial the only source of prepulse data. The

TABLE II. Canine Prostate Gross Lesion Dimensions and Electric Field Thresholds (E_{IRE})

Canine Lesion	Metric	Dimension	E_{IRE} (V/cm)
Lesion site 1	Width	4.8 mm	1000
	Height	4.3 mm	975
Lesion site 2	Width	5.2 mm	950
	Height	5.1 mm	860
Combined volume	—	0.196 cm^3	955
Average E_{IRE}*	—	—	948 ± 53.0

*Presented as mean ± SD.

numerical models were then solved for the five trials investigated experimentally (Fig. 3B–D). The human trials simulated one set of electrode pair pulses performed prior to the other, matching the trials. When simulating the canine 1,250 V electric pulse protocol, the σ_{max} conductivity in $\sigma(E)$ was 0.65 S/m, matching the electric current of 4.8 A. The matched σ_{max} for $\sigma(E)$ in patient one were 0.75 and 1.1 S/m for the two pulse sets, respectively. The second patient had $\sigma_{max} = 0.95$ S/m for both pulse sets, giving an average human σ_{max} of 0.927 ± 0.166 S/m.

Lesion dimensions were correlated with their corresponding electric field threshold for the single canine and two human cases in Table II and Table III, respectively. The overall average lethal electric field threshold was $1{,}072 \pm 119$ V/cm.

An overlay of the experimental canine gross pathological specimen with the numerical model solution was made using GNU Image Manipulation Program (GIMP 2) open-source image editing software (GNU Project, Boston, MA) (Fig. 4). Model results were scaled to the experimental gross pathology by matching the locations of electrode insertion.

DISCUSSION

This study provides important information regarding the translation of irreversible electroporation (IRE) non-thermal targeted ablation towards the treatment of prostate cancer. IRE ablates a volume of tissue without damaging neighboring sensitive structures [13,21]; making it appealing for whole-gland and focal

TABLE III. Human Prostate Histologically Integrated Lesion Volumes and Electric Field Thresholds (E_{IRE})

Subject	Lesion volume (cm^3)	E_{IRE} (V/cm)
Human 1	1.14	1085
Human 2	2.46	1185

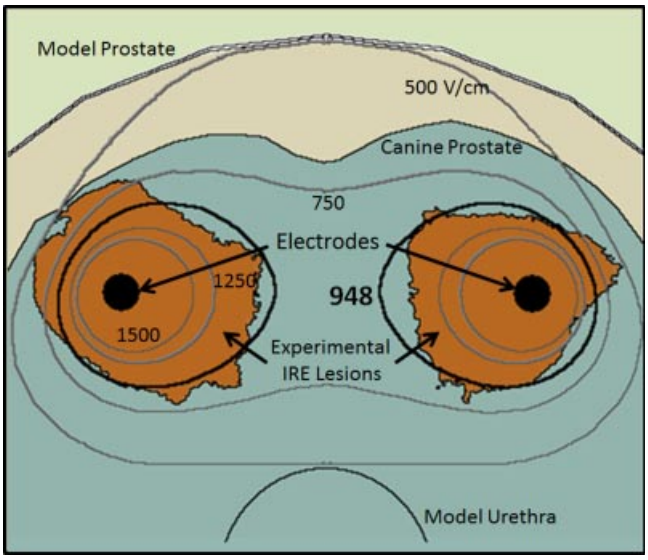

Fig. 4. Comparison of numerical model and gross pathology. Canine prostate trial comparing experimental prostate (blue) and lesions (orange) with numerical simulation domains of (gray) prostate as well as electric field contours (V/cm). Image scales were matched based on electrode locations.

prostate tumor destruction without inducing the high morbidity risks associated with other local prostate cancer therapies. However, therapeutic IRE remains in its infancy, and effects from the electric pulses remain to be characterized in a wide array of tissues, including prostate.

The results here show the effective electric field threshold for healthy prostate tissue ablation is $1{,}072 \pm 119$ V/cm, as evaluated from lesions pathologically examined acutely at 6 hr and 3 or 4 weeks post-IRE. This value is substantially higher than other investigated tissues, including 500 V/cm for healthy brain tissue [34] and 637 V/cm for healthy liver [14], a distinction providing evidence for differential susceptibilities to IRE electric pulses that are organ- or cellular-dependent. It also suggests future work may be necessary to determine IRE effects for applications in different organs and cancer varieties, as opposed to extrapolating existing data from healthy liver lesions. However, until this is completed, existing in vivo studies should offer reasonable general ablation estimates.

It should be noted that this study evaluated lesion dimensions on formalin-preserved tissues, which will slightly reduce lesion dimensions relative to perfused in vivo organs. Although this will alter the predicted electric field threshold, likely increasing it, it is unlikely a substantial enough effect to explain the very distinct IRE threshold described here. This is further supported because many previous ablation lesion tissue characterizations were also evaluated using resected and preserved organs.

The higher electric field threshold found for healthy prostate tissue has multiple potential implications. If prostate tumors also have a higher electric field threshold as a range of 600 to 1300 V/cm was found for cutaneous tumors in [44], then, considerably stronger pulsing protocols must be applied to ensure adequate coverage of the entire targeted region of the tumor plus margin. This correlates with more required electrode insertions, secondary pulse parameters (pulse number and pulse length), and higher voltages. When increasing pulse protocol strength, care must be taken to avoid significant thermal damage, which could limit the ability for IRE to spare of the urethra and neurovascular bundles. This may be done by increasing pulse numbers to reduce necessary electric fields [29], decreasing the pulse delivery rate, and increasing the number of electrode insertions and total number of pulse sets.

Although protocol modifications may be necessary to consider due to prostate resilience to IRE, they do not contraindicate IRE as a valuable therapeutic technique for prostate tumors. This is particularly true when one considers typical prostate sizes (~28 to 35 cm^3) for whole-gland ablation [45], as well as for focal ablation of the prostate tumors, where one study noted 80% of patients undergoing radical prostatectomy had tumors $<2\,cm^3$ [46]. These volumes are smaller than tumors commonly encountered during IRE, including the sarcoma case study (136 cm^3) [24] and the human safety study ($32.8 \pm 63.6\,cm^3$, max $= 357\,cm^3$, min $= 0.524\,cm^3$; assuming spherical tumors) [26]. Smaller required ablation volumes in prostate should readily enable IRE treatment despite higher electric field thresholds.

Conversely, the higher threshold for healthy prostate tissue could be advantageous if prostate tumors are shown to have a lower electric field threshold. Tumors often have significantly different microstructure than their lineage organ; and rapidly dividing cancer cells may be less resilient to the stresses from the IRE-induced membrane defects, requiring less effective pulse protocol strength to be killed. If this is true, IRE prostate tumor treatments could robustly kill all the cancerous cells while much of the healthy prostate survives. This would simplify IRE treatment protocols and improve treatment outcomes. However, such a prospect is speculative, and future work should identify an IRE electric field threshold specifically for prostate tumors.

IRE pulse electrical current is a function of applied voltage as well as electrode exposure length, as shown in Table I. This is because larger exposure lengths utilize a greater volume of tissue for current flow

between the electrodes, reducing the effective resistance of the tissue. Electroporation generators are typically limited to a maximum electrical current, such as the 50 A noted for the ECM830 and the NanoKnife. This results in an upper threshold for applied voltage between a given electrode pair geometry, which may limit maximum ablation dimensions. However, it is possible to reduce the risk for over-current errors by reducing exposure length to keep currents within generator limits at higher voltages, increasing ablation height and width dimensions. In such an approach, pulsing between electrode pairs may be repeated at multiple insertion depths to attain the desired ablation depth dimension as well. This withdrawal-pulse technique is already used in clinical IRE reports [26,27,39,47].

Figure 4 shows the numerically modeled electric field distribution with the calibrated lethal electric field threshold of 948 V/cm for canines, which predicts a greater proportion of the lesion between the electrodes than outside them relative to the experiment. This discrepancy may be due to domain boundary effects, where the modeled electrodes were placed more centrally in the prostate than the actual experimental electrodes, which may have skewed the electric field distribution and altered the lethal region.

This study experimentally and numerically determined electrical conductivity parameters for prostate tissue to use in the asymmetrical sigmoid σ(E) function [42], which can be used for future prostate simulations. However, human trial pre-pulse currents were not recorded, and baseline conductivity, σ_0, was derived solely from the canine data. It is likely that human baseline conductivity will be different. While canine σ_0 was 0.284 S/m, human prostate conductivity at low frequencies is 0.4113 S/m [48]. Future work should record pre-pulse electrical current to refine the optimal human-specific baseline conductivity to use in the models.

There is a difference in calibrated canine σ_0 and σ_{max} parameters here relative to those from the preliminary report in Ref. [33]. This is because the electrodes in the models here were treated as boundaries without a physical electrode domain rather than discrete physical domains. This changed the numerically modeled integrated current density to match the experimental data with more physiological conductivities. Boundary-only electrodes were also employed for human trial simulations.

One promising finding here is that the average human prostate σ_{max} of 0.927 S/m is in good agreement with the β-dispersion equivalent circuit hypothesis [42], where conductivity ranges from 0.783 to 1.06 S/m at frequencies between 10 and 500 MHz, respectively ($\sigma = 0.916$ at 100 MHz) [48]. This supports using this technique to approximate dynamic tissue behavior in response to pulsed electric fields for different tissues. As this approach accumulates support, it may be possible to estimate numerical model parameters in new organs without requiring large animal in vivo experiments, reducing cost and the number of animals required for research.

Lethal electric field thresholds are a function of several pulse parameters. For identical secondary pulse protocol parameters, the electric field offers a simple translational metric to determine ablation volume over a range of electrode geometries and voltages. However, if other pulse parameters are changed; namely pulse length, repetition rate, and total number of pulses, then the required transmembrane potential and corresponding electric field to irreversibly electroporate the cells will also change. While the effects of secondary pulse parameters is the subject of continuing investigation [29,35,49], further work remains to optimize these for practical clinical implementation while maintaining IREs advantages as a structure-sparing modality. Likely, such parameters will be standardized to attain maximum ablation dimensions for a given electrode pair and applied voltage while maintaining procedural pragmatism and minimizing thermal effects that may mitigate some advantages of IRE ablation.

Though all IRE electric field thresholds were much higher here than previously characterized in vivo tissues, the canine protocol threshold (948 V/cm) was slightly lower than that from the human trials (1,085 and 1,185 V/cm). This may be attributable to the differences between secondary pulse parameters. Canine trial parameters were based on experimental evidence and previous tissue characterizations using 100 μsec long pulses and higher pulse numbers; while the human trials were constrained to 90 total pulses, each 70 μsec long. Human trial pulses were delivered at a cardiac-synchronized rate, which is variable. Although in vivo healthy porcine liver ablations suggest that ablation dimension differences attributable to pulse number and pulse length are not statistically significant within the 50–90 total pulse range and 50–100 μsec pulse length [49], a general trend remains possible within the experimental variability. However, despite the potential effect attributable to the secondary parameters between the canine and human trials, all were performed within ranges commonly employed in experimental and clinical trials.

CONCLUSION

This investigation provides valuable preliminary information regarding IRE effects in prostate tissue in the short- and medium-term. Needle electrodes delivered IRE electric pulses into prostates which were harvested 4 hr following pulse delivery for a canine

and 3 or 4 weeks for two human trials. Numerical models simulated the experiments to determine prostate tissue properties when simulating protocols for treatment planning. The σ_{max} of 0.927 S/m determined here matches well with prostate tissue conductivity at β-dispersion frequencies, supporting use of this tissue behavior to estimate conductivity functions in tissues that have not been characterized. Lesion dimensions were correlated with the simulations to determine a lethal electric field threshold of $1{,}072 \pm 119$ V/cm, higher than comparable in vivo studies of other organs, suggesting IRE effects may vary according to tissue and cell variety. The simulation findings can be implemented in improving treatment planning for IRE prostate cancer treatment, a promising application of IRE ablation.

ACKNOWLEDGMENT

This work is supported by the Flack Trustees, The Coulter Foundation, and the Whitaker International Program. Nanoknife system and electrodes donated by Angiodynamics, Inc. The authors thank the staff at the AMREP animal facility, as well as Victoria Earl and Joanne Bergmann and The Alfred Hospital radiology staff for their assistance in performing the experimental and safety study trials. The authors thank Steve Solomon and Jonathan Coleman for critically reviewing the manuscript.

REFERENCES

1. Boukaram C, Hannoun-Levi J-M. Management of prostate cancer recurrence after definitive radiation therapy. Cancer Treat Rev 2010;36(2):91–100.
2. Bomers JG, Sedelaar JP, Barentsz JO, Futterer JJ. MRI-guided interventions for the treatment of prostate cancer. AJR Am J Roentgenol 2012;199(4):714–720.
3. Catalona WJ, Smith DS, Ratliff TL, Basler JW. Detection of organ-confined prostate cancer is increased through prostate-specific antigen-based screening. JAMA 1993;270(8):948–954.
4. Evans SM, Millar JL, Davis ID, Murphy DG, Bolton DM, Giles GG, Frydenberg M, Andrianopoulos N, Wood JM, Frauman AG, Costello AJ, McNeil JJ. Patterns of care for men diagnosed with prostate cancer in Victoria from 2008 to 2011. Med J Aust 2013;198(10):540–545.
5. Nguyen CT, Jones JS. Focal therapy in the management of localized prostate cancer. BJU Int 2011;107(9):1362–1368.
6. Gerritsen WR. The evolving role of immunotherapy in prostate cancer. Ann Oncol 2012;23(suppl 8):viii22–viii27.
7. Bill-Axelson A, Holmberg L, Ruutu M, Garmo H, Stark JR, Busch C, Nordling S, Haggman M, Andersson SO, Bratell S, Spangberg A, Palmgren J, Steineck G, Adami HO, Johansson JE. Radical prostatectomy versus watchful waiting in early prostate cancer. N Engl J Med 2011;364(18):1708–1717.
8. Hakimi AA, Feder M, Ghavamian R. Minimally invasive approaches to prostate cancer: A review of the current literature. Urol J 2007;4(3):130–137.
9. Weaver JC, Chizmadzhev YA. Theory of electroporation: A review. Bioelectrochem Bioenerg 1996;41:135–160.
10. Lee RC. Cell injury by electric forces. Ann N Y Acad Sci 2005;1066:85–91.
11. Davalos R, Mir L, Rubinsky B. Tissue ablation with irreversible electroporation. Ann Biomed Eng 2005;33(2):223–231.
12. Edd JF, Horowitz L, Davalos RV, Mir LM, Rubinsky B. *In vivo* results of a new focal tissue ablation technique: Irreversible electroporation. IEEE Trans Biomed Eng 2006;53(5):1409–1415.
13. Onik G, Mikus P, Rubinsky B. Irreversible electroporation: Implications for prostate ablation. Technol Cancer Res Treat 2007;6(4):295–300.
14. Miklavcic D, Semrov D, Mekid H, Mir LM. A validated model of in vivo electric field distribution in tissues for electrochemotherapy and for DNA electrotransfer for gene therapy. Biochim Biophys Acta 2000;1523(1):73–83.
15. Rubinsky B, Onik G, Mikus P. Irreversible electroporation: A new ablation modality—Clinical implications. Technol Cancer Res Treat 2007;6(1):37–48.
16. Neal RE II, Cheung W, Kavnoudias H, Thomson KR. Spectrum of imaging and characteristics for liver tumors treated with irreversible electroporation. J Biomed Sci and Eng 2012;5(12A): 813–818.
17. Mir LM, Orlowski S. Mechanisms of electrochemotherapy. Adv Drug Deliv Rev 1999;35:107–118.
18. Neal RE II, Rossmeisl JH Jr, Robertson JL, Arena CB, Davis EM, Singh RN, Stallings J, Davalos RV. Improved local and systemic anti-tumor efficacy for irreversible electroporation in immunocompetent versus immunodeficient mice. PLoS ONE 2013;8(5): e64559.
19. Li X, Xu K, Li W, Qiu X, Ma B, Fan Q, Li Z. Immunologic response to tumor ablation with irreversible electroporation. PLoS ONE 2012;7(11):e48749.
20. Lee EW, Loh CT, Kee ST. Imaging guided percutaneous irreversible electroporation: Ultrasound and immunohistological correlation. Technol Cancer Res Treat 2007;6(4):287–293.
21. Maor E, Ivorra A, Leor J, Rubinsky B. The effect of irreversible electroporation on blood vessels. Technol Cancer Res Treat 2007;6(4):307–312.
22. Al-Sakere B, Andre F, Bernat C, Connault E, Opolon P, Davalos RV, Rubinsky B, Mir LM. Tumor ablation with irreversible electroporation. PLoS ONE 2007;2(11):e1135.
23. Neal RE II, Singh R, Hatcher HC, Kock ND, Torti SV, Davalos RV. Treatment of breast cancer through the application of irreversible electroporation using a novel minimally invasive single needle electrode. Breast Cancer Res Treat 2010;123(1):295–301.
24. Neal RE II, Rossmeisl JH Jr, Garcia PA, Lanz OI, Henao-Guerrero N, Davalos RV. Successful treatment of a large soft tissue sarcoma with irreversible electroporation. J Clin Oncol 2011;29(13):e372–e377.
25. Garcia PA, Pancotto T, Rossmeisl JH Jr, Henao-Guerrero N, Gustafson NR, Daniel GB, Robertson JL, Ellis TL, Davalos RV. Non-thermal irreversible electroporation (N-TIRE) and adjuvant fractionated radiotherapeutic multimodal therapy for intracranial malignant glioma in a canine patient. Technol Cancer Res Treat 2011;10(1):73–83.
26. Thomson KR, Cheung W, Ellis SJ, Federman D, Kavnoudias H, Loader-Oliver D, Roberts S, Evans P, Ball C, Haydon A.

Investigation of the safety of irreversible electroporation in humans. J Vasc Interv Radiol 2011;22(5):611–621.

27. Narayanan G, Hosein PJ, Arora G, Barbery KJ, Froud T, Livingstone AS, Franceschi D, Rocha Lima CM, Yrizarry J. Percutaneous irreversible electroporation for downstaging and control of unresectable pancreatic adenocarcinoma. J Vasc Interv Radiol 2012;23(12):1613–1621.
28. Martin RCG, McFarland K, Ellis S, Velanovich V. Irreversible electroporation therapy in the management of locally advanced pancreatic adenocarcinoma. J Am Coll Surgeons 2012;215(3): 361–369.
29. Rubinsky J, Onik G, Mikus P, Rubinsky B. Optimal parameters for the destruction of prostate cancer using irreversible electroporation. J Urol 2008;180(6):2668–2674. Epub 2008 Oct 2631.
30. Neal RE II, Smith RL, Kavnoudias H, Rosenfeldt F, Ou R, Mclean C, Davalos RV, Thomson KR. The effects of metallic implants on electroporation therapies: Feasibility of irreversible electroporation for brachytherapy salvage. Cardiovasc Intervent Radiol 2013;36(6):1638–1645.
31. Neal RE II, Davalos RV. The feasibility of irreversible electroporation for the treatment of breast cancer and other heterogeneous systems. Ann Biomed Eng 2009;37(12):2615–2625.
32. Ivorra A, Rubinsky B. In vivo electrical impedance measurements during and after electroporation of rat liver. Bioelectrochemistry 2007;70(2):287–295. Epub 2006 Oct 2021.
33. Neal RE II, Kavnoudias H, Rosenfeldt F, Ou R, Marron J, Davalos RV, Thomson KR. In vivo validation of irreversible electroporation electric field threshold for prostate tissue. ASME 2013 Summer Bioengineering Conference. Sunriver, OR, USA; 2013.
34. Garcia P, Rossmeisl J, Neal R, Ellis T, Olson J, Henao-Guerrero N, Robertson J, Davalos R. Intracranial nonthermal irreversible electroporation: In vivo analysis. J Membr Biol 2010;236(1):127–136.
35. Pucihar G, Krmelj J, Rebersek M, Napotnik TB, Miklavcic D. Equivalent pulse parameters for electroporation. IEEE Trans Biomed Eng 2011;58(11):3279–3288. doi: 3210.1109/TBME.2011.2167232. Epub 2162011 Sep 2167236.
36. Shafiee H, Garcia PA, Davalos RV. A preliminary study to delineate irreversible electroporation from thermal damage using the arrhenius equation. J Biomech Eng 2009;131(7):074509.
37. Appelbaum L, Ben-David E, Sosna J, Nissenbaum Y, Goldberg SN. US findings after irreversible electroporation ablation: radiologic–pathologic correlation. Radiology 2012;262(1): 117–125.
38. Ball C, Thomson KR, Kavnoudias H. Irreversible electroporation: A new challenge in "Out of Operating Theater" anesthesia. Anesth Analg 2010;110(5):1305–1309.
39. Kingham TP, Karkar AM, D'Angelica MI, Allen PJ, Dematteo RP, Getrajdman GI, Sofocleous CT, Solomon SB, Jarnagin WR, Fong Y. Ablation of perivascular hepatic malignant tumors with irreversible electroporation. J Am Coll Surg 2012;215(3):379–387.
40. Lee RC, Zhang D, Hannig J. Biophysical injury mechanisms in electrical shock trauma. Ann Rev Biomed Eng 2000;2(1):477–509.
41. Sel D, Cukjati D, Batiuskaite D, Slivnik T, Mir LM, Miklavcic D. Sequential finite element model of tissue electropermeabilization. IEEE Trans Biomed Eng 2005;52(5):816–827.
42. Neal RE II, Garcia PA, Robertson JL, Davalos RV. Experimental characterization and numerical modeling of tissue electrical conductivity during pulsed electric fields for irreversible electroporation treatment planning. IEEE Trans Biomed Eng 2012;59(4):1076–1085. Epub 2012 Jan 1076.
43. Gabriel S, Lau RW, Gabriel C. The dielectric properties of biological tissues: II. Measurements in the frequency range 10 Hz to 20 GHz. Phys Med Biol 1996;41(11):2251–2269.
44. Qin Z, Jiang J, Long G, Lindgren B, Bischof JC. Irreversible electroporation: An in vivo study with dorsal skin fold chamber. Ann Biomed Eng 2013;41(3):619–629.
45. Zhang SJ, Qian HN, Zhao Y, Sun K, Wang HQ, Liang GQ, Li FH, Li Z. Relationship between age and prostate size. Asian J Androl 2013;15(1):116–120. doi: 110.1038/aja.2012.1127. Epub 2012 Dec 1010.
46. Chan LW, Stamey TA. Calculating prostate cancer volume preoperatively: The D'Amico equation and some other observations. J Urol 1998;159(6):1998–2003.
47. Martin RC II, McFarland K, Ellis S, Velanovich V. Irreversible electroporation in locally advanced pancreatic cancer: Potential improved overall survival. Ann Surg Oncol 2012;6:6.
48. Duck FA. Physical properties of tissue: A comprehensive reference book. New York: Academic Press; 1990.
49. Ben-David E, Appelbaum L, Sosna J, Nissenbaum I, Goldberg SN. Characterization of irreversible electroporation ablation in in vivo porcine liver. AJR Am J Roentgenol 2012;198(1):W62–W68.